ACSNANO

www.acsnano.org

ARTICLE

Control of Raman Scattering Quantum Interference Pathways in Graphene

Xue Chen, Sven Reichardt, Miao-Ling Lin, Yu-Chen Leng, Yan Lu, Heng Wu, Rui Mei, Ludger Wirtz,* Xin Zhang,* Andrea C. Ferrari, and Ping-Heng Tan*

Cite This: *ACS Nano* 2023, 17, 5956–5962

Read Online

ACCESS | Metrics & More | Article Recommendations

ABSTRACT: **Graphene is an ideal platform to study the coherence of quantum interference pathways by tuning doping or laser excitation energy. The latter produces a Raman excitation profile that provides direct insight into the lifetimes of intermediate electronic excitations and, therefore, on quantum interference, which has so far remained elusive. Here, we control the Raman scattering pathways by tuning the laser excitation energy in graphene doped up to 1.05 eV. The Raman excitation profile of the G mode indicates its position and full width at half-maximum are linearly dependent on doping. Doping-enhanced electron−electron interactions dominate the lifetimes of Raman scattering pathways and reduce Raman interference. This will provide guidance for engineering quantum pathways for doped graphene, nanotubes, and topological insulators.**

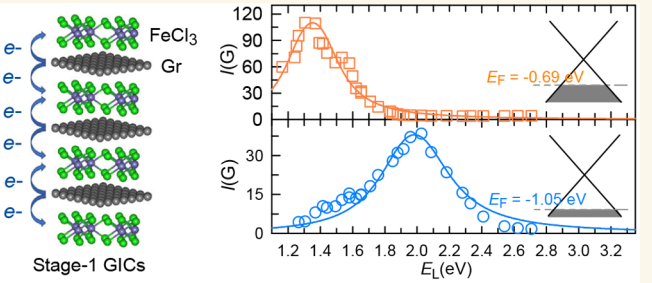

KEYWORDS: *quantum interference, resonant Raman scattering, electron−electron interaction, electron−phonon coupling, graphite intercalation compounds*

Interference between quantum pathways can occur in all physical systems,[1] as demonstrated by electron collisions,[2] conductance jumps,[3] transmission dips,[4−6] exciton transports,[7] magnetoconductance,[8] chemical reaction dynamics,[9] and inelastic light scattering.[10−12] In the quantum picture of the Raman scattering process,[13] incident photons (energy E_L) induce electronic excitations, which then generate phonons, followed by the radiation of scattered photons. The intermediate electronic excitations act as quantum pathways, thus they can interfere with each other. As E_L is tuned to approach the electronic transition of interest, resonant Raman scattering (RRS) occurs,[13] greatly enhancing some quantum pathways,[14] therefore the Raman intensity.[10,15] The ability to control quantum pathways could be used to detect,[10] understand,[11,16] and exploit[12,17] inelastic light scattering, and to design quantum interference-based devices.[3−6]

The effect of quantum interference on the intensity of Raman modes was reported in Si,[18] CdS,[18] carbon nanotubes,[11,19] graphene,[10,14−16,20−23] $MoTe_2$,[24,25] and ReS_2.[17] The linear band structure of single layer graphene (SLG) makes it ideal to study quantum interference,[10,14−16,20,22,23] as it enables continuous control of the Raman scattering pathways, by tuning the electrostatic doping, E_F, relative to a fixed E_L,[10,15,16,21,22] or, conversely, tuning E_L under a fixed E_F.[26] Such E_F or E_L handle enables optical control of the intermediate electronic excitations.[10] Raman experiments in SLG showed enhanced G and D peak intensities for E_F approaching $0.5E_L$.[10,16] The enhancement was limited to 7 in Refs 16 and 21 due to defects and inhomogeneous dopants introduced by ionic gel dielectrics. We previously showed that $FeCl_3$ intercalation into graphite can produce SLG flakes without defects with E_F up to ~ -1 eV,[27] achieving a high carrier concentration $\sim 7.56 \times 10^{13}$ cm^{-2}. Here, we use this to control the intermediate electronic excitations by tuning E_L for heavily doped SLG with fixed E_F.

Performing Raman measurements by tuning E_L produces the so-called Raman excitation profile (REP), i.e., a plot of intensity of Raman modes as a function of E_L.[13] This allows one to directly monitor the lifetimes of intermediate electronic excitations, because the REP width is a signature of electronic energy broadening, i.e., it is proportional to the inverse lifetime of Raman scattering pathways.[28] These can be modified by

Received: January 6, 2023
Accepted: February 24, 2023
Published: March 10, 2023

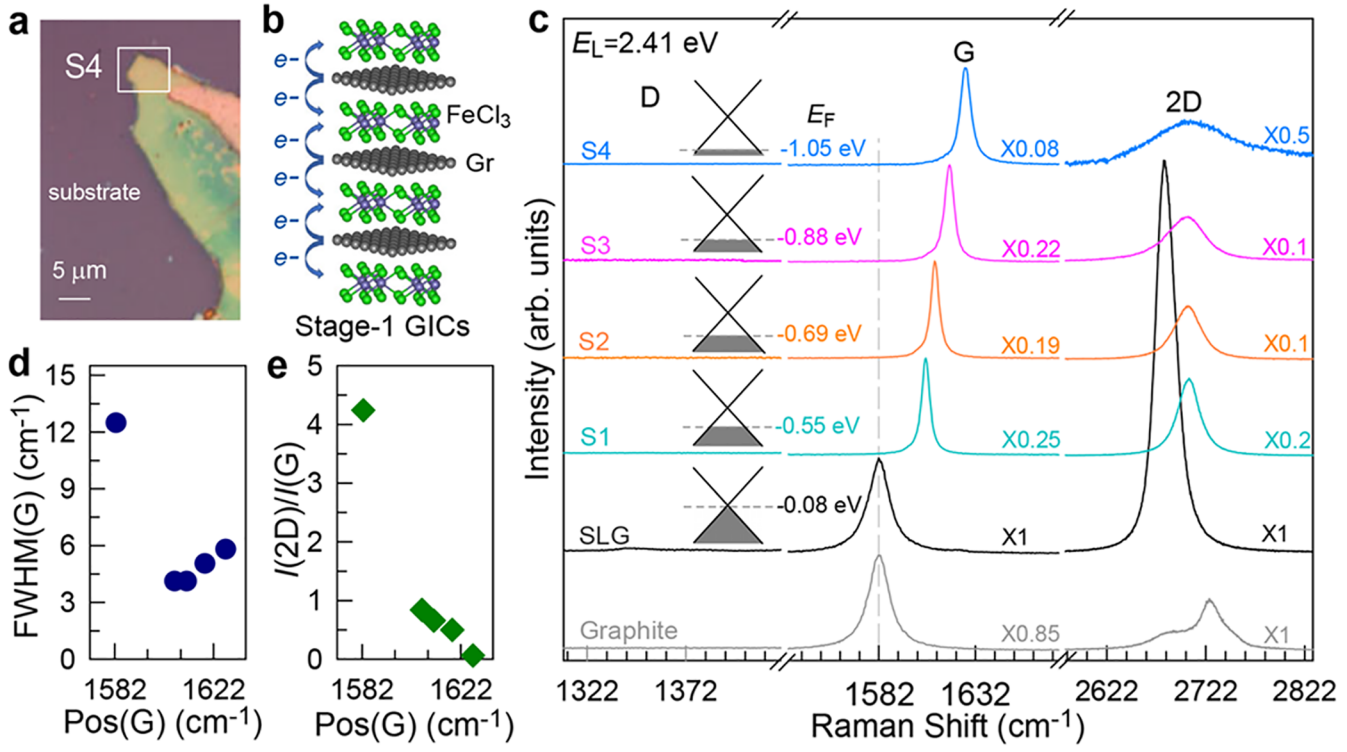

Figure 1. (a) Optical image of sample S4, with the area of interest indicated by the white box. (b) Schematic illustration of intercalation process,[27] where Cl, Fe, and C atoms are color coded in green, purple, and dark-gray, respectively. (c) Raman spectra of samples S1−S4, with different E_F, SLG ($E_F \sim -0.08$ eV) and graphite, for $E_L = 2.41$ eV. (d) FWHM(G) and (e) $I(2D)/I(G)$ as a function of Pos(G) for SLG in samples S1−S4.

electron−electron (e−e) interactions[29,30] and electron−phonon (e−ph) coupling.[31] Their effects on Raman scattering pathways and overall quantum interference have not been investigated thus far, to the best of our knowledge.

Here, we control quantum interference of Raman scattering pathways in SLG by tuning E_L in hole (h)-doped SLG produced by intercalating $FeCl_3$ into graphite.[27] The G peak REP features a single resonant peak, whose position depends linearly on E_F. The full width at half-maximum (FWHM) of the G peak REP also depends linearly on E_F. We show that such doping-induced REP broadening is determined by the Raman scattering pathways lifetime and is dominated by e−e interactions, enhanced by carrier concentration. This shows that E_L can be used to control the allowed Raman scattering pathways in SLG. In principle, quantum interference is always present in Raman scattering from any materials, with the exact form of e−e and e−ph interactions depending on their electronic structure. Thus, besides SLG and topological insulators with Dirac-like band structure, one can expect to control Raman scattering pathways in intercalated or substitution-doped few-layer graphene, metallic nanotubes, and anisotropic layered materials.

RESULTS AND DISCUSSION

Raman Spectroscopy of Doped Graphene. We prepare 4 heavily doped SLG samples (denoted S1−S4) by intercalating $FeCl_3$ into bulk graphite, as for Ref 27 (see Methods). Figure 1a is a representative optical image of one sample (S4). Figure 1a shows regions with different colors (pink, green, and light-yellow), as a result of different doping and layer thickness.[27] We thus take Raman measurements only on regions with uniform color, so as to probe uniform doping regions. Figure 1b shows a schematic of $FeCl_3$-intercalated trilayer graphene, resulting in 3 individual heavily doped SLG sandwiched by $FeCl_3$ layers.

Figure 1c plots the 2.41 eV Raman spectra of S1−S4, not intentionally doped SLG, and graphite. In the not intentionally doped SLG, the 2D to G intensity and areas ratios are $I(2D)/I(G) \sim 4.2$ and $A(2D)/A(G) \sim 8.4$, respectively, indicating h-doping with $E_F \sim -0.08$ eV.[30,32] We also see extremely weak peaks ~1342 cm^{-1} and ~1622 cm^{-1} corresponding to defect activated D and D′ peaks.[22] We take this non-intentionally doped SLG as representing intrinsic SLG. For S1−S4, the Pos(G) and Pos(2D) blueshift is a signature of doping.[22,32,33] E_F can be estimated by combining Pos(G), Pos(2D), FWHM(G), $I(2D)/I(G)$, and $A(2D)/A(G)$[22,30,32,33] as ~ −0.55, −0.69, −0.88, −1.05 eV, respectively. Photoexcited hot carriers in doped SLG when $2|E_F|$ approaches E_L result in broadband luminescence, with peak position slightly lower than $2|E_F|$, as discussed in Ref 10. For S4 with $E_F \sim -1.05$ eV, the Stokes Raman scattering 2D peak energy is ~2.1 eV, close to $2|E_F|$, thus resulting in a photoluminescence (PL) background, as shown in Figure 5. The sharp G peak can be distinguished well from the broad PL background. We then subtract the PL background, to give Figure 1c. We note that the asymmetrical line shape of S4 in Figure 1c is the result of the broadband PL.

Quantum Interference and Raman Excitation Profile. As E_L ranges from 1.5 to 2.7 eV, the experimental $I(G)$ in graphite and intrinsic SLG is almost constant when normalized to the Raman signals of calcium fluoride or cyclohexane[34,35], due to cancellation of destructive interference among different

https://doi.org/10.1021/acsnano.3c00180
ACS Nano 2023, 17, 5956−5962

pathways.[10,15] For a fixed E_L, a strong increase of $I(G)$ occurs as $|E_F|$ is tuned close to $E_L/2$,[10] due to Pauli blocking of destructive quantum interference.[10,15]

Figure 2a plots Raman measurements of S4 ($E_F \sim -1.05$ eV) from 1.26 to 2.71 eV over 26 steps: 1.26, 1.31, 1.37, 1.42,

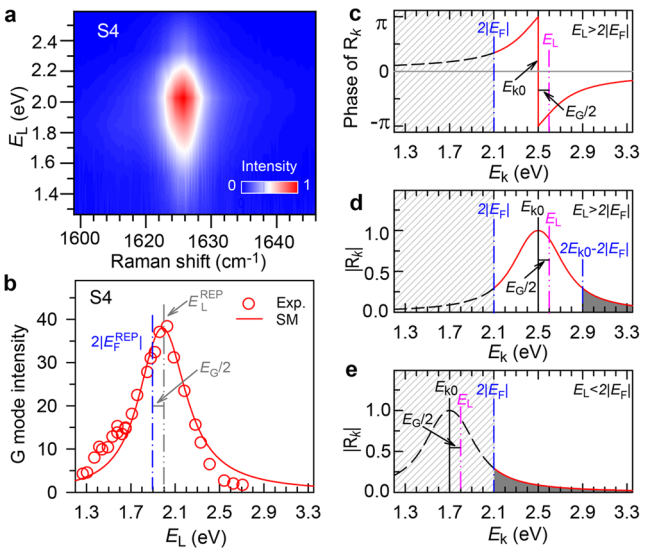

Figure 2. (a) Contour plots of $I(G)$ of S4 as a function of Pos(G) and E_L. (b) Experimental G REP and fit based on eq 1. Calculated (c) phase of R_k and (d) magnitude $|R_k|$ for each pathway at E_L = 2.6 eV and γ = 0.225 eV for SLG with $2|E_F|$= 2.1 eV. (e) Calculated $|R_k|$ for E_L = 1.8 eV. The diagonal and shaded areas indicate the blocking region imposed by the Pauli exclusion principle and the pathways contributing to $I(G)$.

1.44, 1.49, 1.53, 1.58, 1.65, 1.62, 1.65, 1.71, 1.76, 1.85, 1.88, 1.92, 1.96, 2.03, 2.09, 2.18, 2.28, 2.33, 2.41, 2.54, 2.62, 2.71 eV. $I(G)$ is normalized to that of bulk graphite. All the spectra in Figure 2a have FWHM(G) as narrow as 5.8 cm^{-1}, because e−ph scattering is forbidden by Pauli blocking once $|E_F|$ is larger than half the G peak energy, $E_G/2$;[22,27,32,33] therefore, we consider $I(G)$ to determine the G REP in Figure 2b. In contrast to the E_L-insensitive $I(G)$ in intrinsic SLG,[34,35] Figure 2b indicates that $I(G)$ depends on E_L, reaching a maximum for $E_L \sim 2$ eV, close to $2|E_F|$.

To explain the G REP in doped SLG, we calculate $I(G)$ as a first-order Raman scattering process with e interacting only through mean-field potentials:[13]

$$I(G) = \left| \sum_{k} M_k R_k \right|^2 \quad (1)$$

where $R_k = 1/[(E_L - E_k + i\gamma)(E_L - E_G - E_k + i\gamma)]$ is the resonance factor, E_k the vertical electronic transition energy at wavevector k, γ is the energy broadening of the excited state, comprising contributions from e−e interactions (γ^{ee}) and e−ph coupling (γ^{ep}),[28,30] and M_k is a third-order transition matrix element (see Methods). R_k refers to one of the Raman scattering pathways.[10] When summing over k, the pathways interfere with each other, which leads to a constructive or destructive effect on $I(G)$, depending on the phase of allowed pathways.[10,15]

We first consider a simplified model (SM) with M_k in eq 1 constant for all k. In this case, $I(G) \propto |\sum_k R_k|^2$. Figures 2c,d plots the calculated phase and magnitude of R_k under E_L = 2.6 eV and γ = 0.225 eV, fitted as discussed below. An abrupt change in the phase (from π to $-\pi$) is observed at $E_{k_0} = E_L - E_G/2$, which makes the other nonresonant scattering pathways antisymmetric in phase, relative to E_{k_0}. For intrinsic SLG, all quantum pathways interfere destructively, leading to a weak $I(G)$, as shown in Figure 1c. However, in doped SLG, those pathways with $E_k < 2|E_F|$ are Pauli blocked,[10,27] as for the diagonal pattern in Figures 2c,d with $2|E_F|$ = 2.1 eV. Thus, the corresponding antisymmetric pathways with $E_k > 2E_{k_0} - 2|E_F|$ (shaded region in Figure 2d) will contribute to the $I(G)$ enhancement. The G REP peak occurs at $E_L = 2|E_F| + E_G/2$, denoted as E_L^{REP}. In this case, all allowed scattering pathways are in-phase. As E_{k_0} lies in the blocking region of $2|E_F|$, Figure 2e, the number of allowed in-phase pathways becomes smaller when E_L is farther from $2|E_F|$, and the corresponding overall $I(G)$ signal is weaker. Therefore, by changing E_L, one can control the allowed Raman scattering pathways, creating a REP peak (Figure 2b).

Based on the SM, the REP peak occurs at $E_L^{REP} = 2|E_F| + E_G/2$. This allows us to define E_F according to the observed E_L^{REP}, i.e., $2E_F^{REP} = E_L^{REP} - E_G/2$. As illustrated by the vertical lines in Figure 2b, $|E_F^{REP}|$ is ∼0.95 eV for S4, consistent with that extracted from Pos(G), Pos(2D), $I(2D)/I(G)$, and $A(2D)/A(G)$. $|E_F^{REP}|$ determines the lower bound in the k summation of eq 1 to reproduce the experimental REP. The solid line in Figure 2b is the fitted curve to the experimental REP with $\gamma = 0.225 \pm 0.04$ eV, and it is larger than $\gamma \sim 0.13$ eV for SLG with $E_F \sim 0.5$ eV on 300 nm-SiO_2/Si.[30]

Effects of Electron−Electron Interaction. Figure 3a depicts the experimental REPs of S1−S4 measured by varying E_L from 1.26 to 2.71 eV. Due to the increasing E_F from S1, −0.55 eV, to S4, −1.05 eV, the corresponding E_L^{REP} blue-shifts. Based on the experimental E_L^{REP}, E_F^{REP} of S2−S4 can be determined as ∼ −0.63, −0.84, −0.95 eV, respectively,

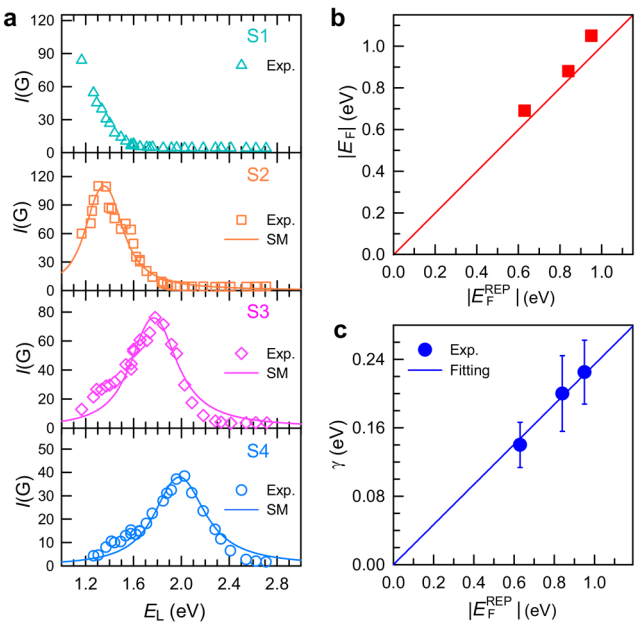

Figure 3. (a) Experimental REPs for S1−S4 along with the fitted curves based on eq 1. (b) Correlation between $|E_F^{REP}|$ and $|E_F|$. The solid line corresponds to $|E_F^{REP}| = |E_F|$. (c) γ as a function of $|E_F^{REP}|$. The solid line is a linear fit.

https://doi.org/10.1021/acsnano.3c00180
ACS Nano 2023, 17, 5956−5962

consistent with E_F from Pos(G), Pos(2D), I(2D)/I(G), and A(2D)/A(G) (Figure 3b).

The fitted γ from REPs of S2−S4 with eq 1 increase monotonically with $|E_F^{REP}|$, i.e., $\gamma = 0.234|E_F^{REP}|$ (Figure 3c). γ is related to the broadening of excited states, due to the interactions with elementary excitations, such as doping-induced e/h, ph, and defects.[30] Since S2−S4 are defect-free, as shown from the absence of the D peaks in Figure 1c, we can write $\gamma = \gamma^{ee} + \gamma^{ep}$.[30] γ^{ee} denotes the e−e scattering rate, which increases as more e/h are added to SLG. $\gamma^{ee} = 2|E_F|f(e^2/2\varepsilon_0\varepsilon\hbar\nu_F)$, where ε_0, ε, $\hbar$, and ν_F are the vacuum permittivity, dielectric constant, Planck's constant, and Fermi velocity, respectively.[30] From Ref 30, we get $f \sim 0.09$,[27] i.e., $\gamma^{ee} = 0.18|E_F|$, smaller than the fitted slope ~0.234 in Figure 3c. On the other hand, γ^{ep} does not depend explicitly on E_F. From Ref 28, γ^{ep} is dispersive with E_k, as $\gamma^{ep} = 0.021E_k - 0.0034$. This must be considered when summing $\boldsymbol{k}$ in eq 1. However, since the slope of the dispersion, ~0.021, is $\ll 1$, γ^{ep} can be approximated to $\gamma^{ep} \sim 0.042|E_F|$ (see Methods). The overall slope of γ is ~0.22, in agreement with the fit in Figure 3c. Thus, the REP energy broadening in doped SLG comes mainly from enhanced e−e interactions.

We now use *ab initio* density functional and many-body perturbation theory to calculate the full Raman scattering matrix-element $\mathcal{M}_{\boldsymbol{k}}$ ($\mathcal{M}_{\boldsymbol{k}} = M_{\boldsymbol{k}}R_{\boldsymbol{k}}$) on the independent-particle level (see Methods). Figure 4a plots the dispersion of the full scattering matrix element and compares it with the SM (Figure 4b) for E_L = 2 eV. The constant dipole and e−ph matrix elements (EPMEs) are individually set to the square root of their average modulus squared taken over bands, polarizations, and the resonant $\boldsymbol{k}$-point surface. The full matrix element is much more dispersive than in the SM, which only shows the two peaks at the surface of resonant $\boldsymbol{k}$-points. We attribute the more pronounced resonance peaks in the full calculation to two effects: (i) the underestimation of the decay of the dipole and EPMEs far away from the Brillouin Zone (BZ) edge at the K-point in the SM and (ii) the finite scattering matrix element at the K-point in the SM vanishes in the full calculations, because the phase of the numerator in eq 1 is constant, rather than rotating around K, in line with approximate angular momentum conservation.[14,15] Thus, the SM captures the largest part of the physics through its almost double-resonant structure, but leads to a quantitative underestimation of resonance effects. The full calculated REP for S4 is normalized to the experimental data (Figure 4c). This is slightly broadened as compared to the SM, improving the agreement on the red-side of the resonance peak in the experimental REP.

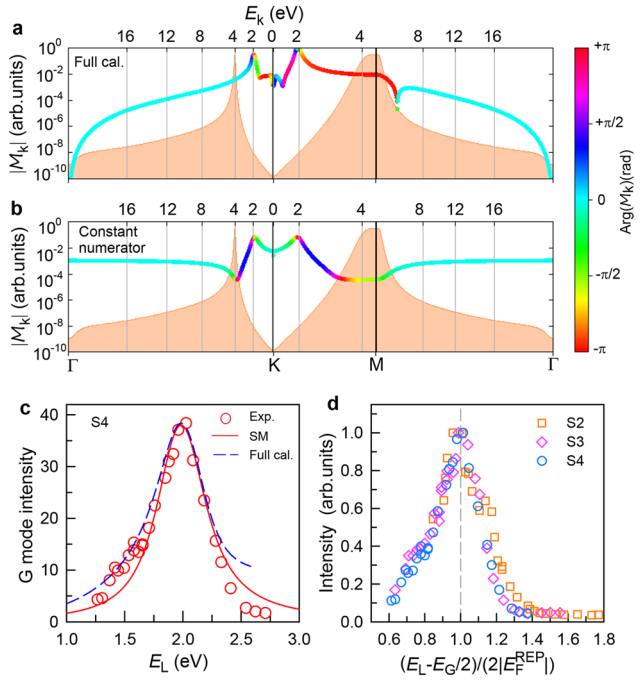

Figure 4. Absolute value (logarithmic scale) and phase (color-encoded) of $\mathcal{M}_{\boldsymbol{k}}$ ($\mathcal{M}_{\boldsymbol{k}} = M_{\boldsymbol{k}}R_{\boldsymbol{k}}$) in the high-symmetry line Γ − K − M − Γ at E_L = 2 eV by including M_k (a) (Full cal.), and setting the dipole and EPMEs to a constant (b) (Constant numerator), both for a constant broadening of γ = 0.225 eV. The shaded area represents the value of the joint density of states at E_k. (c) Experimental REP (open circles) and theoretical REPs calculated by *ab initio* (Full cal., dashed line) and the SM (solid line). (d) Rescaled experimental REPs for S2−S4 as a function of $(E_L - E_G/2)/2|E_F^{REP}|$.

The fitted γ from REPs is linear with $|E_F^{REP}|$, as indicated in Figure 3c. The quantum interference among Raman scattering pathways mainly depends on E_k away from $2E_L - 2|E_F| - E_G$ ($E_L > 2|E_F|$) or $2|E_F|(E_L < 2|E_F|)$ (Figures 2d, e), which can be finely tuned by E_L or E_F. The established relations of $2|E_F^{REP}| = E_L^{REP} - E_G/2$ can now be used to rescale E_L of the REPs in Figure 3a. The corresponding rescaled REPs, i.e., I(G) as a function of $(E_L - E_G/2)/2|E_F^{REP}|$, are in Figure 4d for S2−S4. The 3 rescaled REPs show a similar profile, although their E_F^{REP} is different, confirming the linear dependence of γ on E_F, as for the Raman measurements in Figure 3a.

CONCLUSIONS

We carried out a systematic experimental study of quantum interference effects on the Raman scattering pathways of the G mode in doped SLG. By adjusting E_L over 26 individual energies between 1.2 and 2.7 eV, we controlled the number of Raman scattering pathways, in order to enhance or attenuate I(G), reaching a maximum for $E_L = 2|E_F| + E_G/2$. The dispersive γ can be fitted from the experimental REPs, and is linearly related to E_F, with the main contribution dominated by e−e interactions. REPs can be rescaled by $E_L^{REP} = 2|E_F^{REP}| + E_G/2$. Thus, REP is a powerful tool for probing electronic interactions.

METHODS

Sample Preparation. The vapor transport method is exploited to fabricate $FeCl_3$-based stage-1 GICs, as for Refs 27 and 36. $FeCl_3$ powder (Sinopharm Chemical Reagent Co., Ltd.) and micromechanically exfoliated graphite flakes (Kish graphite from Graphene Supermarket) are deposited on Si covered with 90 nm SiO_2 and positioned in the different zones of a glass tube. This is then pumped to ~1.5 × 10^{-4} Torr and heated at 393 K for 30 min to keep the $FeCl_3$ anhydrous. Next, the glass tube is sealed and placed in the furnace with a reaction temperature of 613 K for 30 h. The samples are then immediately exposed to air. Gaseous $FeCl_3$ fills the whole sealed glass tube during the intercalating process, thus the position of the starting bulk graphite has negligible effect on doping concentration, which is controlled by the amount of $FeCl_3$ in the tube.[27]

Raman Measurements. Raman spectra are measured using a Jobin-Yvon HR800 micro-Raman system equipped with 1200 and 1800 grooves/mm gratings, coupled with a liquid-nitrogen-cooled charge coupled device or an InGaAs array detector and a 50×

https://doi.org/10.1021/acsnano.3c00180
ACS Nano 2023, 17, 5956−5962

objective lens with a numerical aperture of 0.55. We use E_L = 1.16, 1.88, 2.33 eV from diode-pumped solid-state lasers, 1.24−1.58 eV from a tunable continuous-wave Ti:Saphire laser, 1.96, 2.03, 2.09, 2.28 eV from He−Ne lasers, 1.83, 1.92, 2.18 eV from a Krypton ion laser, and 2.41, 2.54, 2.62, 2.71 eV from an Ar ion laser. The laser power is kept <2 mW to avoid sample heating. During measurements at each E_L, the G peak of a graphite flake with thickness ∼100 nm is measured under the same experimental conditions to normalize the S1−S4 G peak intensity, I(G), for the calibrated REPs.[34,35] In order to investigate the asymmetrical line shape of the 2D mode, Raman spectra of samples S1−S4 and not intentionally doped SLG are collected in a broad energy range, for E_L = 2.41 eV with 100 grooves/mm grating, as shown in Figure 5. Note that these spectra without any background subtraction are shifted for comparison.

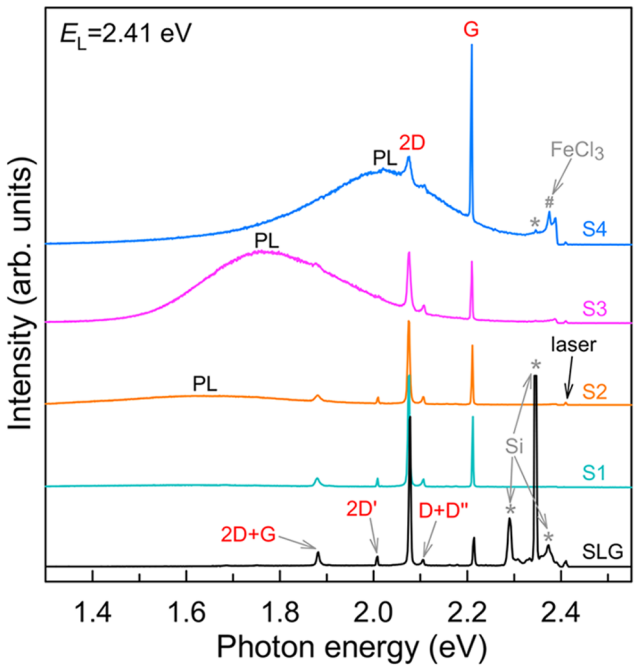

Figure 5. Raman spectra of samples S1−S4 and unintentionally doped SLG with no background subtracted, for E_L = 2.41 eV. The Raman peaks of graphene are identified as well as those from $FeCl_3$ and Si substrate labeled by gray # and *, respectively. The broadband backgrounds in samples S2−S4 are PL emission near $2|E_F|$ of heavily doped SLG.[10]

Full *Ab Initio* Calculations. *Ab initio* calculations of the Raman matrix elements are done as for Refs 14 and 37. The SLG band structure, e-light, and the screened e−ph matrix elements are obtained from density functional (perturbation) theory, with the PWscf code from Quantum ESPRESSO[38,39] using a plane-wave basis set with an energy cutoff of 80 Ry. An ultrasoft pseudopotential is used to describe the e-ion interaction, while the mean-field exchange−correlation potential is approximated on the level of the generalized gradient approximation in the parametrization by Perdew, Burke, and Ernzerhof.[40] A vacuum spacing of 14 Å separates periodic SLG copies, with the relaxed value of 2.46 Å for the lattice constant.[14] A uniform 60 × 60 × 1 $\boldsymbol{k}$-point mesh is used to sample the first BZ in a self-consistent calculation for the ground state density and potential, and for the calculation of the change of the self-consistently screened lattice potential with the ph displacement. Due to the SLG semimetallic nature, the latter requires a thermal smearing, for which the electronic states are populated according to a Fermi−Dirac distribution with temperature corresponding to 0.002 Ry. To obtain converged results for the Raman intensity, the electronic π and π^* and the optical and e−ph matrix elements are interpolated to a dense 480 × 480 × 1 $\boldsymbol{k}$-point mesh using maximally localized Wannier functions from a coarse 12 × 12 × 1 $\boldsymbol{k}$-point grid, as implemented in the Wannier90[41] and EPW codes.[42,43] The full *ab initio* calculation goes beyond the approximation of retaining the almost double-resonant term in eq 1, for which $M_k = d^i_{k,\pi^*\pi}\,(g^\lambda_{k,\pi^*\pi^*} - g^\lambda_{k,\pi\pi})(d^i_{k,\pi^*,\pi})^*$, where $d^i_{k,\pi^*\pi}$ denotes the i-th component of the dipole matrix element and $g^\lambda_{k,nn}$ denotes the diagonal screened e−ph matrix element for band n = π,π^* for ph polarization λ = x,y. Instead, it includes all possible time orderings of the independent-particle three-particle correlation.[37]

Effective FWHM of an Ideal REP. For simplicity, E_G is ignored in eq 1. Then, $\Delta = E_k - E_L = E_k - E_{k_0}$, where $E_L = E_{k_0}$ applies since E_G is not included. Thus, the dispersive $\gamma = \beta E_k$ can be arranged as $\gamma = \beta\Delta + \gamma_0$, where $\gamma_0 = \beta E_{k_0}$. Thus, the sum over $\boldsymbol{k}$ is equivalent to integrating over Δ, giving:

$$I(G) = \left|\sum_{\boldsymbol{k}} R_{\boldsymbol{k}}\right|^2 = \left|\int \frac{1}{[\Delta + i(\beta\Delta + \gamma_0)]^2} d\Delta\right|^2 = \frac{1}{(\beta^2+1)^2}\frac{1}{\left(\Delta + \frac{\beta\gamma_0}{\beta^2+1}\right)^2 + \left(\frac{\gamma_0}{\beta^2+1}\right)^2} \quad (2)$$

The maximum $I(G)$ $[I(G)^{max}]$ is $1/\gamma_0^2$ and the FWHM of the profile is $2\gamma_0/(\beta^2+1)$. Since $\beta = 0.021 \ll 1$,[28] the FWHM is approximated by $2\gamma_0 = 2\beta E_{k_0}$, only related to γ at E_{k_0}. Eq 2 then simplifies to $I(G) = 1/(\Delta^2 + \gamma_0^2)$, which is exactly the same as setting γ as a constant, since:

$$I(G) = \left|\int \frac{1}{(\Delta + \mathrm{i}C)^2} d\Delta\right|^2 = \frac{1}{\Delta^2 + C^2} \quad (3)$$

with C replaced by γ_0. This suggests that the constant γ widely used in the literature[10,16] comes from γ_0 defined at E_{k_0}. The area of the profile can be further obtained by multiplying $I(G)^{max}$ by the FWHM, which is $2/\gamma_0$.

In doped SLG, $E_{k_0} = 2|E_F|$. Thus, $\gamma^{ep} = 0.021E_k - 0.0034$ gives $\gamma^{ep} = 0.042|E_F| - 0.0034 \sim 0.042|E_F|$.

AUTHOR INFORMATION

Corresponding Authors

Ludger Wirtz − *Department of Physics and Materials Science, University of Luxembourg, Luxembourg 1511, Luxembourg;* orcid.org/0000-0001-5618-3465; Email: ludger.wirtz@uni.lu

Xin Zhang − *State Key Laboratory of Superlattices and Microstructures, Institute of Semiconductors, Chinese Academy of Sciences, Beijing 100083, China; Center of Materials Science and Optoelectronics Engineering and CAS Center of Excellence in Topological Quantum Computation, University of Chinese Academy of Sciences, Beijing 100049, China;* Email: zhangxin@semi.ac.cn

Ping-Heng Tan − *State Key Laboratory of Superlattices and Microstructures, Institute of Semiconductors, Chinese Academy of Sciences, Beijing 100083, China; Center of Materials Science and Optoelectronics Engineering and CAS Center of Excellence in Topological Quantum Computation, University of Chinese Academy of Sciences, Beijing 100049, China;* orcid.org/0000-0001-6575-1516; Email: phtan@semi.ac.cn

Authors

Xue Chen − *State Key Laboratory of Superlattices and Microstructures, Institute of Semiconductors, Chinese Academy of Sciences, Beijing 100083, China; Center of*

https://doi.org/10.1021/acsnano.3c00180
ACS Nano 2023, 17, 5956−5962

Materials Science and Optoelectronics Engineering and CAS Center of Excellence in Topological Quantum Computation, University of Chinese Academy of Sciences, Beijing 100049, China

Sven Reichardt − *Department of Physics and Materials Science, University of Luxembourg, Luxembourg 1511, Luxembourg;* orcid.org/0000-0003-3014-004X

Miao-Ling Lin − *State Key Laboratory of Superlattices and Microstructures, Institute of Semiconductors, Chinese Academy of Sciences, Beijing 100083, China;* orcid.org/0000-0001-5838-8237

Yu-Chen Leng − *State Key Laboratory of Superlattices and Microstructures, Institute of Semiconductors, Chinese Academy of Sciences, Beijing 100083, China*

Yan Lu − *State Key Laboratory of Superlattices and Microstructures, Institute of Semiconductors, Chinese Academy of Sciences, Beijing 100083, China*

Heng Wu − *State Key Laboratory of Superlattices and Microstructures, Institute of Semiconductors, Chinese Academy of Sciences, Beijing 100083, China; Center of Materials Science and Optoelectronics Engineering and CAS Center of Excellence in Topological Quantum Computation, University of Chinese Academy of Sciences, Beijing 100049, China*

Rui Mei − *State Key Laboratory of Superlattices and Microstructures, Institute of Semiconductors, Chinese Academy of Sciences, Beijing 100083, China; Center of Materials Science and Optoelectronics Engineering and CAS Center of Excellence in Topological Quantum Computation, University of Chinese Academy of Sciences, Beijing 100049, China*

Andrea C. Ferrari − *Cambridge Graphene Centre, University of Cambridge, Cambridge CB3 0FA, United Kingdom;* orcid.org/0000-0003-0907-9993

Complete contact information is available at: https://pubs.acs.org/10.1021/acsnano.3c00180

Notes

The authors declare no competing financial interest.

ACKNOWLEDGMENTS

We thank W. L. Ma for fruitful discussions. We acknowledge support from the National Natural Science Foundation of China (grant nos. 12127807, 12004377, and 12174381), CAS Key Research Program of Frontier Sciences (grant nos. ZDBS-LY-SLH004 and XDPB22), CAS Project for Young Scientists in Basic Research (YSBR-026), and the National Reasearch Fund (FNR) Luxembourg, project "RESRAMAN" (grant no. C20/MS/14802965), EU Graphene Flagship, ERC grants Hetero2D, GIPT, EU grants Graph-X, CHARM, EPSRC grants EP/K01711X/1, EP/K017144/1, EP/N010345/1, EP/L016087/1, EP/V000055/1, EP/X015742/1, the Youth Innovation Promotion Association, Chinese Academy of Sciences (No. 2023125).

REFERENCES

(1) Ficek, Z.; Swain, S. *Quantum Interference and Coherence: Theory and Experiments*; Springer: New York, 2005; Chapter 1, pp 1−44.

(2) Liu, R. C.; Odom, B.; Yamamoto, Y.; Tarucha, S. Quantum Interference in Electron Collision. *Nature* **1998**, *391*, 263−265.

(3) Zheng, H.; Hou, S.; Xin, C.; Wu, Q.; Jiang, F.; Tan, Z.; Zhou, X.; Lin, L.; He, W.; Li, Q.; Zheng, J.; Zhang, L.; Liu, J.; Yang, Y.; Shi, J.; Zhang, X.; Zhao, Y.; Li, Y.; Lambert, C.; Hong, W. Room-Temperature Quantum Interference in Single Perovskite Quantum Dot Junctions. *Nat. Commun.* **2019**, *10*, 5458.

(4) Guédon, C. M.; Valkenier, H.; Markussen, T.; Thygesen, K. S.; Hummelen, J. C.; van der Molen, S. J. Observation of Quantum Interference in Molecular Charge Transport. *Nat. Nanotechnol.* **2012**, *7*, 305−309.

(5) Bai, J.; Daaoub, A.; Sangtarash, S.; Li, X.; Tang, Y.; Zou, Q.; Sadeghi, H.; Liu, S.; Huang, X.; Tan, Z.; Liu, J.; Yang, Y.; Shi, J.; Meszaros, G.; Chen, W.; Lambert, C.; Hong, W. Anti-Resonance Features of Destructive Quantum Interference in Single-Molecule Thiophene Junctions Achieved by Electrochemical Gating. *Nat. Mater.* **2019**, *18*, 364−369.

(6) Greenwald, J. E.; Cameron, J.; Findlay, N. J.; Fu, T.; Gunasekaran, S.; Skabara, P. J.; Venkataraman, L. Highly Nonlinear Transport Across Single-Molecule Junctions via Destructive Quantum Interference. *Nat. Nanotechnol.* **2021**, *16*, 313−317.

(7) Glazov, M. M. Quantum Interference Effect on Exciton Transport in Monolayer Semiconductors. *Phys. Rev. Lett.* **2020**, *124*, 166802.

(8) Stojetz, B.; Miko, C.; Forró, L.; Strunk, C. Effect of Band Structure on Quantum Interference in Multiwall Carbon Nanotubes. *Phys. Rev. Lett.* **2005**, *94*, 186802.

(9) Xie, Y.; Zhao, H.; Wang, Y.; Huang, Y.; Wang, T.; Xu, X.; Xiao, C.; Sun, Z.; Zhang, D. H.; Yang, X. Quantum Interference in H+HD → H_2+D Between Direct Abstraction and Roaming Insertion Pathways. *Science* **2020**, *368*, 767−771.

(10) Chen, C.-F.; Park, C.-H.; Boudouris, B. W.; Horng, J.; Geng, B.; Girit, C.; Zettl, A.; Crommie, M. F.; Segalman, R. A.; Louie, S. G.; Wang, F. Controlling Inelastic Light Scattering Quantum Pathways in Graphene. *Nature* **2011**, *471*, 617.

(11) Duque, J. G.; Telg, H.; Chen, H.; Swan, A. K.; Shreve, A. P.; Tu, X.; Zheng, M.; Doorn, S. K. Quantum Interference Between the Third and Fourth Exciton States in Semiconducting Carbon Nanotubes Using Resonance Raman Spectroscopy. *Phys. Rev. Lett.* **2012**, *108*, 117404.

(12) Gu, P.; Tan, Q.; Wan, Y.; Li, Z.; Peng, Y.; Lai, J.; Ma, J.; Yao, X.; Yang, S.; Yuan, K.; Sun, D.; Peng, B.; Zhang, J.; Ye, Y. Photoluminescent Quantum Interference in a van der Waals Magnet Preserved by Symmetry Breaking. *ACS Nano* **2020**, *14*, 1003−1010.

(13) Pinczuk, A.; Burstein, E. *Light Scattering in Solids I*; Springer-Verlag: Berlin, Heidelberg, 1983; Chapter 2, pp 25−75.

(14) Reichardt, S.; Wirtz, L. *Ab Initio* Calculation of the G peak Intensity of Graphene: Laser-Energy and Fermi-Energy Dependence and Importance of Quantum Interference Effects. *Phys. Rev. B* **2017**, *95*, 195422.

(15) Basko, D. M. Calculation of the Raman G Peak Intensity in Monolayer Graphene: Role of Ward Identities. *New J. Phys.* **2009**, *11*, 095011.

(16) Liu, J.; Li, Q.; Zou, Y.; Qian, Q.; Jin, Y.; Li, G.; Jiang, K.; Fan, S. The Dependence of Graphene Raman D-Band on Carrier Density. *Nano Lett.* **2013**, *13*, 6170−6175.

(17) Zhang, S.; Huang, J.; Yu, Y.; Wang, S.; Yang, T.; Zhang, Z.; Tong, L.; Zhang, J. Quantum Interference Directed Chiral Raman Scattering in Two-Dimensional Enantiomers. *Nat. Commun.* **2022**, *13*, 1254.

(18) Ralston, J. M.; Wadsack, R. L.; Chang, R. K. Resonant Cancelation of Raman Scattering From CdS and Si. *Phys. Rev. Lett.* **1970**, *25*, 814−818.

(19) Liu, K.; Hong, X.; Wu, M.; Xiao, F.; Wang, W.; Bai, X.; Ager, J. W.; Aloni, S.; Zettl, A.; Wang, E.; Wang, F. Quantum-Coupled Radial-Breathing Oscillations in Double-Walled Carbon Nanotubes. *Nat. Commun.* **2013**, *4*, 1375.

(20) Maultzsch, J.; Reich, S.; Thomsen, C. Double-Resonant Raman Scattering in Graphite: Interference Effects, Selection Rules, and Phonon Dispersion. *Phys. Rev. B* **2004**, *70*, 155403.

(21) Kalbac, M.; Reina-Cecco, A.; Farhat, H.; Kong, J.; Kavan, L.; Dresselhaus, M. S. The Influence of Strong Electron and Hole Doping on the Raman Intensity of Chemical Vapor-Deposition Graphene. *ACS Nano* **2010**, *4*, 6055−6063.

(22) Ferrari, A. C.; Basko, D. M. Raman Spectroscopy as a Versatile Tool for Studying the Properties of Graphene. *Nat. Nanotechnol.* **2013**, *8*, 235−246.
(23) Hasdeo, E. H.; Nugraha, A. R. T.; Dresselhaus, M. S.; Saito, R. Fermi Energy Dependence of First- and Second-Order Raman Spectra in Graphene: Kohn Anomaly and Quantum Interference Effect. *Phys. Rev. B* **2016**, *94*, 075104.
(24) Golasa, K.; Grzeszczyk, M.; Molas, M. R.; Zinkiewicz, M.; Bala, L.; Nogajewski, K.; Potemski, M.; Wysmolek, A.; Babinski, A. Resonant Quenching of Raman Scattering Due to Out-of-Plane A_{1g}/A_1' Modes in Few-Layer $MoTe_2$. *Nanophotonics* **2017**, *6*, 1281−1288.
(25) Miranda, H. P. C.; Reichardt, S.; Froehlicher, G.; Molina-Sanchez, A.; Berciaud, S.; Wirtz, L. Quantum Interference Effects in Resonant Raman Spectroscopy of Single- and Triple-Layer $MoTe_2$ From First-Principles. *Nano Lett.* **2017**, *17*, 2381−2388.
(26) Bonacum, J. P.; O'Hara, A.; Bao, D.-L.; Ovchinnikov, O. S.; Zhang, Y.-F.; Gordeev, G.; Arora, S.; Reich, S.; Idrobo, J.-C.; Haglund, R. F.; Pantelides, S. T.; Bolotin, K. I. Atomic-Resolution Visualization and Doping Effects of Complex Structures in Intercalated Bilayer Graphene. *Phys. Rev. Mater.* **2019**, *3*, 064004.
(27) Zhao, W.-J.; Tan, P.-H.; Liu, J.; Ferrari, A. C. Intercalation of Few-Layer Graphite Flakes with $FeCl_3$: Raman Determination of Fermi Level, Layer by Layer Decoupling, and Stability. *J. Am. Chem. Soc.* **2011**, *133*, 5941−5946.
(28) Venezuela, P.; Lazzeri, M.; Mauri, F. Theory of Double-Resonant Raman Spectra in Graphene: Intensity and Line Shape of Defect-Induced and Two-Phonon Bands. *Phys. Rev. B* **2011**, *84*, 035433.
(29) Hwang, E. H.; Hu, B. Y.-K.; Das Sarma, S. Inelastic Carrier Lifetime in Graphene. *Phys. Rev. B* **2007**, *76*, 115434.
(30) Basko, D. M.; Piscanec, S.; Ferrari, A. C. Electron-Electron Interactions and Doping Dependence of The Two-Phonon Raman Intensity in Graphene. *Phys. Rev. B* **2009**, *80*, 165413.
(31) Basko, D. M. Theory of Resonant Multiphonon Raman Scattering in Graphene. *Phys. Rev. B* **2008**, *78*, 125418.
(32) Das, A.; Pisana, S.; Chakraborty, B.; Piscanec, S.; Saha, S.; Waghmare, U.; Novoselov, K.; Krishnamurthy, H.; Geim, A.; Ferrari, A.; et al. Monitoring Dopants by Raman Scattering in an Electrochemically Top-Gated Graphene Transistor. *Nat. Nanotechnol.* **2008**, *3*, 210−215.
(33) Pisana, S.; Lazzeri, M.; Casiraghi, C.; Novoselov, K. S.; Geim, A. K.; Ferrari, A. C.; Mauri, F. Breakdown of the Adiabatic Born-Oppenheimer Approximation in Graphene. *Nat. Mater.* **2007**, *6*, 198−201.
(34) Cançado, L. G.; Jorio, A.; Pimenta, M. A. Measuring the Absolute Raman Cross Section of Nanographites as a Function of Laser Energy and Crystallite Size. *Phys. Rev. B* **2007**, *76*, 064304.
(35) Klar, P.; Lidorikis, E.; Eckmann, A.; Verzhbitskiy, I. A.; Ferrari, A. C.; Casiraghi, C. Raman Scattering Efficiency of Graphene. *Phys. Rev. B* **2013**, *87*, 205435.
(36) Dresselhaus, M. S.; Dresselhaus, G. Intercalation Compounds of Graphite. *Adv. Phys.* **2002**, *51*, 1−186.
(37) Reichardt, S.; Wirtz, L. Nonadiabatic Exciton-Phonon Coupling in Raman Spectroscopy of Layered Materials. *Sci. Adv.* **2020**, *6*, eabb5915.
(38) Giannozzi, P.; Baroni, S.; Bonini, N.; Calandra, M.; Car, R.; Cavazzoni, C.; Ceresoli, D.; Chiarotti, G. L.; Cococcioni, M.; Dabo, I.; Dal Corso, A.; de Gironcoli, S.; Fabris, S.; Fratesi, G.; Gebauer, R.; Gerstmann, U.; Gougoussis, C.; Kokalj, A.; Lazzeri, M.; Martin-Samos, L.; et al. QUANTUM ESPRESSO: a Modular and Open-Source Software Project for Quantum Simulations of Materials. *J. Phys.: Condens. Matter* **2009**, *21*, 395502.
(39) Giannozzi, P.; Andreussi, O.; Brumme, T.; Bunau, O.; Buongiorno Nardelli, M.; Calandra, M.; Car, R.; Cavazzoni, C.; Ceresoli, D.; Cococcioni, M.; Colonna, N.; Carnimeo, I.; Dal Corso, A.; de Gironcoli, S.; Delugas, P.; DiStasio, R. A., Jr; Ferretti, A.; Floris, A.; Fratesi, G.; Fugallo, G.; et al. Advanced Capabilities for Materials Modelling With Quantum ESPRESSO. *J. Phys.: Condens. Matter* **2017**, *29*, 465901.
(40) Perdew, J. P.; Burke, K.; Ernzerhof, M. Generalized Gradient Approximation Made Simple. *Phys. Rev. Lett.* **1996**, *77*, 3865.
(41) Mostofi, A. A.; Yates, J. R.; Pizzi, G.; Lee, Y.-S.; Souza, I.; Vanderbilt, D.; Marzari, N. An Updated Version of Wannier 90: A Tool for Obtaining Maximally-Localised Wannier Functions. *Comput. Phys. Commun.* **2014**, *185*, 2309−2310.
(42) Giustino, F.; Cohen, M. L.; Louie, S. G. Electron-Phonon Interaction Using Wannier Functions. *Phys. Rev. B* **2007**, *76*, 165108.
(43) Poncé, S.; Margine, E. R.; Verdi, C.; Giustino, F. EPW: Electron-Phonon Coupling, Transport and Superconducting Properties Using Maximally Localized Wannier Functions. *Comput. Phys. Commun.* **2016**, *209*, 116−133.

https://doi.org/10.1021/acsnano.3c00180
ACS Nano 2023, 17, 5956−5962